MOUNTAIN-PLAINS CONSORTIUM

MPC 16-306 | R. Bridgelall, Y. Huang, Z. Zhang, and D. Tolliver

A Sensor Fusion Approach to Assess Pavement Condition and Maintenance Effectiveness

A Sensor Fusion Approach to Assess Pavement Condition and Maintenance Effectiveness

Dr. Raj Bridgelall (PI)[1]
Dr. Ying Huang (Co-PI)[2]
Zhiming Zhang[2]
Dr. Denver D. Tolliver[1]

[1]Upper Great Plains Transportation Institute
[2]Department of Civil Engineering
North Dakota State University
Fargo, North Dakota

Disclaimer

The contents of this report reflect the views of the authors, who are responsible for the facts and the accuracy of the information presented. This document is disseminated under the sponsorship of the Department of Transportation, University Transportation Centers Program, in the interest of information exchange. The U.S. Government assumes no liability for the contents or use thereof.

ABSTRACT

Transportation agencies use a variety of methods to evaluate the condition of pavements and the characteristics of their use. Methods range from in-pavement sensors to ride quality characterizations that require specially instrumented probe vehicles. However, the extensive labor, specialized training, and high cost associated with the large variety of existing approaches limit their ability to scale in frequency and coverage. Infrequent monitoring diminishes the accuracy of assessing infrastructure needs and of evaluating maintenance effectiveness. This research developed a sensing approach that extends the capability of in-pavement sensors beyond their ability to measure just loading and condition parameters. Specifically, the approach links the output of durable in-pavement strain sensors to common roughness indices. However, to maintain their accuracy throughout the life cycle of the pavement, models that use their output must be calibrated periodically. Therefore, this research also developed a localized roughness measurement method based on connected vehicle sensing to calibrate the models. Field experiments validated that the relative roughness indices of the two methods agreed within 3.3%. This result demonstrates that it is possible to build smart roads with embedded strain sensors that can also report roughness levels continuously, without requiring special probe vehicles.

TABLE OF CONTENTS

LIST OF TABLES

LIST OF FIGURES

EXECUTIVE SUMMARY

The United States has the largest road network in the world. The network consisted of more than 2,646,000 miles of paved roads in 2012 and it plays a significant role in the economy, defense, and mobility. The performance evaluation of such a vast network and the capacity to maintain the roadways has become increasingly difficult. In particular, transportation agencies in rural and cold regions face enormous challenges keeping up with demands to repair roads quickly. Agencies must assure consistent repair quality assessment during the short construction season, especially for roads that now support intense industrial activities in oilfields and rural freight corridors. Maintaining a state-of-good repair in these regions requires continuous condition and performance measures in all weather conditions, and without disrupting traffic flows. Pavement condition assessment includes reporting the roughness indices, in-pavement strains and stresses, vehicle weights, traffic volume, and numerous other parameters. However, transportation agencies characterize very few pavements in terms of these parameters because of the high complexity and cost of measuring them.

Embedded strain sensors have the capacity to monitor mechanistic parameters that relate to pavement condition as well as usage levels such as vehicle weights, speeds, and traffic volume. Historically, existing embedded sensors such as electrical strain gauges and electromagnetic loops have failed early in the life cycle of pavement assets. In previous research, this team developed more rugged and reliable devices by packaging optical fiber sensors in three dimensions using fiber-reinforced polymer (FRP) to withstand the harsh environments within pavements. Testing showed that such devices operate robustly within pavements to provide reliable and real-time strain and temperature measurements. Hence, the main idea of this research was to develop a method of deriving pavement roughness indices directly from the output of the embedded optical strain sensors. However, such sensors require periodic calibration to an external measurement of roughness. Therefore, a second idea was to develop a roughness localization and quantification technique that uses connected vehicle sensors. Subsequently, a fusion of the two methods enabled in-pavement optical sensors to effectively monitor continuously a wide variety of pavement mechanistic parameters, traffic load parameters, as well as roughness indices.

Field experiments revealed that without calibration the roughness indices reported by the embedded optical sensors and the connected vehicle methods agreed within 3.3%. This result demonstrates that it is possible to build smart roads that can measure and report their own roughness levels via in-pavement strain sensors. In particular, a fusion of connected vehicle sensing methods and in-pavement sensors will enable smart cities to implement lower-cost, simpler, and more scalable solutions that provide continuous, network-wide assessments of pavement performance and maintenance needs. Future extensions of the method would include a fusion of embedded sensors and autonomous vehicle sensors to aid navigation in bad weather. In future work, the authors will explore those ideas and also extend the method for road condition monitoring and traffic data collection.

1.   INTRODUCTION

Sustained economic development has led to a large increase in roadway transportation. Traffic loads play a critical role in the performance and deterioration of pavements. Hence, the weight of heavy vehicles has been a critical factor in the design and maintenance of roads. Existing in-pavement sensors that can monitor stresses and strains tend to fail early in the asset life cycle (Zhang, Huang and Palek, et al. 2015). However, the authors have previously developed more rugged and reliable sensors by packaging optical fiber sensors in three dimensions using fiber-reinforced polymer (FRP) to withstand the harsh environments within pavements (Zhou, et al. 2012). Testing showed that such devices operate robustly within pavements to provide reliable and real-time strain measurements (Zhang, Huang and Palek, et al. 2015. Such sensors can also measure the volume and weight of vehicles traversing specific road segments (Zhiming, et al. 2015).

In addition to monitoring pavement loading conditions and internal strains, agencies must also characterize and report pavement ride quality in terms of the international roughness index (IRI). However, persistent funding gaps hamper the scaling of existing methods to evaluate roadway performance and condition more regularly. The high cost of deploying specially instrumented vehicles to produce the IRI limits ride quality characterizations to relatively small portions of the network. Therefore, in previous research, the authors developed a connected vehicle method to provide continuous ride quality assessments for all roadways, including local and unpaved roads (R. Bridgelall 2014).

The United States Department of Transportation (USDOT) and equivalent agencies worldwide are collaborating with nearly all vehicle manufacturers to deploy connected vehicles, automated vehicles, and other smart city concepts to assure a steady pace of technology-enabled transportation systems (USDOT 2015). The connected vehicle standard prescribes architectures and methods that would allow remote systems to access the data from sensors that are already aboard regular vehicles. Such sensors include accelerometers, speedometers, odometers, and conventional global positioning system (GPS) receivers. With relatively few connected vehicles currently deployed, researchers have been using the equivalent sensors embedded on smartphones to develop future applications, including methods of pavement performance evaluations (R. Bridgelall 2015).

The main idea of this research was to develop a method that would derive pavement roughness indices directly from the output of embedded optical strain sensors. However, such sensors require periodic calibration to an independent measure of roughness. Therefore, a second idea was to develop a technique that would enable connected vehicles to report localized roughness. Subsequently, a remote processor could calibrate roughness models based on the optical sensor output. Figure 1.1 illustrates the overall approach and the main steps in the process. The in-pavement sensors measure and report both static and dynamic strains continuously. The occasional connected vehicle will measure and report surface roughness by a remote system that is accessible via the Internet and cloud-computing architectures. The remote computer will convert connected vehicle sensor data to roughness indices and use those to calibrate a roughness model based on the optical sensor data. The remote processing will use several models that integrate the optical sensor data to produce a variety of performance and condition measures continuously.

In summary, a fusion of two methods (embedded sensors and connected vehicles) will enable models that use in-pavement optical sensors to continuously monitor pavement mechanistic parameters, traffic load parameters, as well as roughness indices throughout the life cycle of the asset. The availability of both in-pavement sensor and connected vehicle methods of continuous performance and condition evaluations provide agencies with a variety of options to scale an optimum mix of solutions throughout the network.
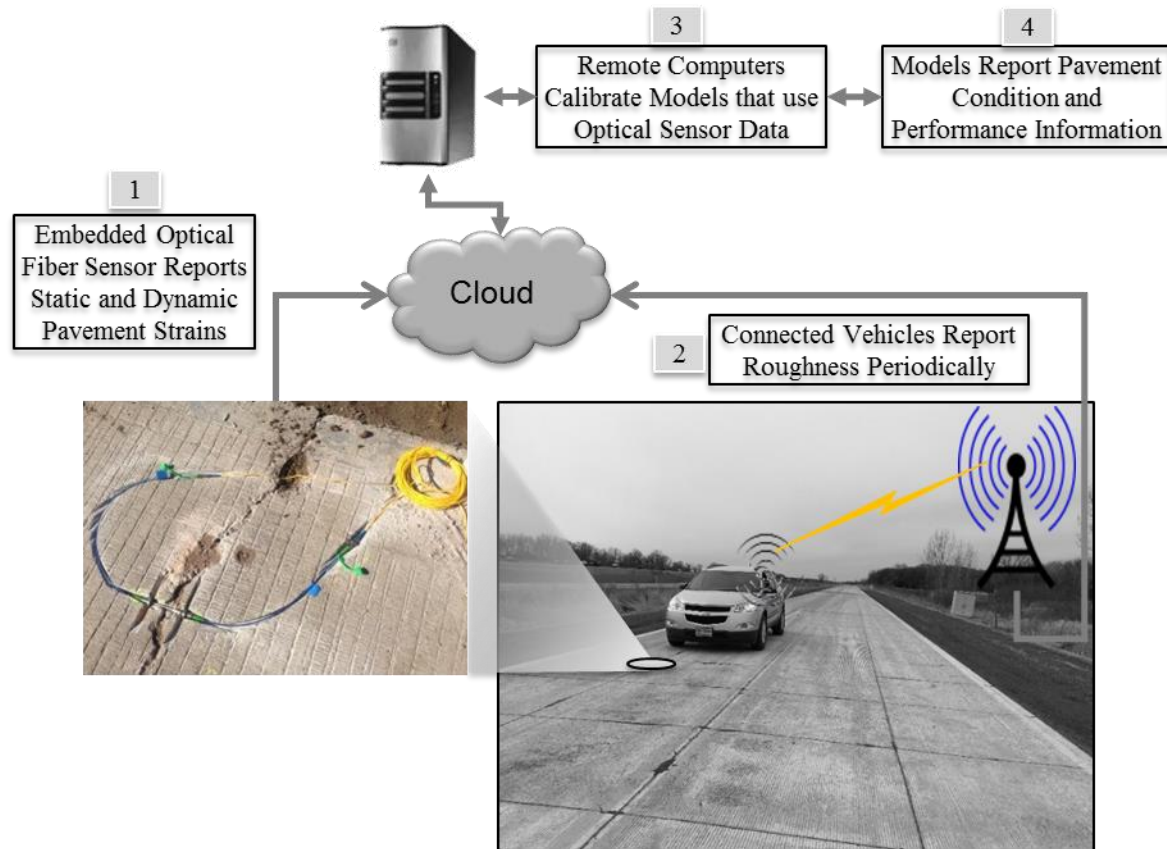
Figure 1.1 System Concepts and Processes

Section 2 of this report summarizes a review of the literature that focuses on methods of characterizing pavement roughness. It is evident that nearly all of the techniques are based on external measurements or probe vehicles. Hence, the idea of using embedded sensors to characterize pavement roughness is unique. Section 3.1 reviews the operating principles, design, and construction of the embedded optical sensors, and develops a framework to optimize the digital interface that will record and communicate the sensor data. Section 3.2 develops a theory that relates the strains measured by in-pavement sensors to a roughness index. Section 3.3 develops the roughness localization technique using the connected vehicle method of characterizing ride quality. Section 4 addresses the optimal deployment design by characterizing the sensitivity of the roughness estimation to the sensor interval placement and sensor signal quality. Section 5 describes the field experiments and case study that validates the approach. Finally, Section 6 provides the conclusions and outlines the potential future work.

2.   LITERATURE REVIEW

Roughness is a global measure of roadway serviceability that has long been one of the major criteria for road condition assessment to guide resource allocation and maintenance planning. The ASTM E867 standard defines roughness as "the deviation of a surface from a true planar surface with characteristic dimensions that affect vehicle dynamics and ride quality" (ASTM 1997). Pavement roughness adversely affects ride quality (Deusen 1967) (Brickman, et al. 1972), vehicle wear (Abaynayaka, et al. 1976), and transportation safety (Gillespie and Sayers, Role of road roughness in vehicle ride 1981). The higher dynamic axle loading from roughness accelerates pavement deterioration (Saleh, Mamlouk and Owusu-Antwi 2000). Rough roads can also increase fuel consumption by as much as 5% (Klaubert 2001).

Researchers and organizations proposed many different roughness statistics to describe the severity of pavement roughness; however, the IRI is the most widely used (ASTM 2015). The IRI computation relies on a mathematical model called a quarter-car. This model simulates the response of a serially coupled damped mass-spring system to estimate the vertical motions of equivalent wheel-assembly masses. The IRI is the accumulated absolute rate difference between the simulated sprung and un-sprung mass motions per unit of distance travelled.

Another important characterization of roughness is the power spectral density (PSD). It is a mathematical representation of the spatial wavelength composition of road profiles rather than a summary index of roughness (Marcondes, et al. 1991). Researchers found that most pavement profiles such as road and runway surfaces have very similar PSD shapes. This observation has led to the use of coefficients that fit exponential functions to the PSD shapes as alternative summaries of roughness. Less frequently used methods also exist. These include the profile index method, which is the root-mean square of a band-pass filtered road profile (Smith, et al. 1997), the ride number method, which is a transformation of the elevation profile per the ASTM E-1489 standard (ASTM 1998), and the root mean square of vertical acceleration approach, which is a statistical method based on the rate of the grade change of the longitudinal profile (McKenzie and Srinarawat 1978).

Roughness measuring methods fall into three major classes (Huang 1993). Class I uses the traditional longitudinal surveys by rod and level or by some other laborsaving apparatus that requires walking along the test path. The Class II techniques measure the road profile with various types of profilometers such as the Chloe-type rolling straightedge (Huang 1993). Class III is an indirect measuring method described as a response-type road roughness meters (RTRRM) that most highway agencies used until the mid-1980s or as an inertial road profiler that began in the 1960s (Brown, Liu and Henning 2010). The RTRRM devices measure the response of the vehicle to the road profile using transducers to accumulate the vertical movement of the axle with respect to the vehicle's body. This method directly reflected the users' ride quality experience. However, variations in suspension characteristics and speed result in measurement inconsistencies. Such approaches also do not provide a sample of the pavement longitudinal profile for spectral analysis.

The inertial road profiling methods use instrumented vehicles to collect road roughness data (Karamihas, Measuring, Characterizing, and Reporting Pavement Roughness of Low-Speed and Urban Roads 2016). Inertial profilers collect pavement condition data at highway speeds and record sufficient data to evaluate the spectral content of the pavement profile. This benefit has led to a substantial increase of countries adopting the method. The principal components of a high-speed profiler include laser-based height sensors, accelerometers, and an accurate distance measuring system. The height sensors record the distance from the base of the vehicle to the pavement surface. Accelerometers above the height sensors record the vertical acceleration of the sensor to correct for reference plane bounces. In theory, double integration of the vertical acceleration signal would recover the vertical displacement of the vehicle. Practically, however, noise and initial conditions tend to create additional issues that limit their use in

urban and local roads where the profiling vehicle must travel at low speeds and accommodate stop-and-go conditions (Karamihas, Measuring, Characterizing, and Reporting Pavement Roughness of Low-Speed and Urban Roads 2016). Nevertheless, in more ideal settings such as freeways, the inertial profiler equipment produces a longitudinal profile of the pavement from the two height measurements.

In addition to the profilers, more cost-effective approaches have evolved based on mobile computing (Hyman, et al. 1990) and other automated data collection techniques that involve more complex sensors (McGhee 2004). Although reports (NCHRP Report 334) indicate that most agencies now use inertial profilers (Hyman, et al. 1990), the literature has very little information about their cost to acquire, operate, and maintain. One study reported the contracted pavement profile data collection and analysis costs ranged from $2.23/mile to $10.00/mile, with an average of $6.12/mile (McGhee 2004). However, the reported costs did not include overhead such as contract administration, equipment maintenance, and equipment depreciation. In more recent developments, researchers have been investigating alternative methods of roughness data collection that would use accelerometers and geospatial position sensors aboard connected vehicles (R. Bridgelall, Connected Vehicle Approach for Pavement Roughness Evaluation 2014).

In general, the relatively high expense and labor requirements of existing approaches prevent agencies from monitoring large portions of their roadway network more often than once annually. Thus, they often make maintenance and rehabilitation decisions based on outdated roughness data. In addition, infrequent roughness measurements preclude the identification of dangerous distress symptoms such as frost heaves that appear and disappear between annual monitoring cycles. These situations result in roadway safety gaps that increase liability.

In addition to the roughness measurements, many agencies developed models to predict road performance using measured distress information for both flexible and rigid pavements. The distress information includes strain data, cracking condition, spalling, pop out, scaling, and a variety of other visible symptoms. The AASHTO and FHWA successfully modeled roughness indices such as the IRI or PSR using key pavement distress information (Paterson 1989) (Yu, et al. 1998) (Darter and Barenberg. 1976) (Al-Omari and Darter 1994) (Carey and Irick 1960). Among various models, empirical and mechanistic analysis have identified several pavement design features and site conditions, including the pavement's temperature, moisture, and axle load cycles that affect the roughness of flexible pavements (Paterson 1989) (Sebaaly, Lani and Hand 1995) (Kajner, Kurlanda and Sparks 1996). NCHRP developed the prediction models for rigid pavements by assembling all the available distress databases and considering their initial IRI (Schram and Abdelrahman 2006). Though many of those factors are a result of pavement strains, none of the previous studies related the IRI directly to the strain distribution inside pavements by mechanistic analysis alone without using statistical models. Such mechanistic-empirical models provide a prediction of the roughness progression but not a direct measure of the actual roughness.

Agencies require a direct measure of the actual pavement roughness as the pavement ages to guide effective maintenance and rehabilitation decisions. Therefore, this paper introduces an approach to evaluate and report the real-time pavement roughness by linking the output of in-pavement strain sensors to the IRI and other roughness indices. This method requires initial installation of the durable strain sensors inside the pavements. During road operation, the sensors report strain data that indicate the level of structural deterioration. The method developed in this study will subsequently produce the IRI by relating the vertical displacement of the pavement to the strain data. An ability to recover the elevation profile using this method also provides a generalized approach for linking it to other summary roughness indices. After installation and calibration, the sensors will provide real-time roughness monitoring continuously, throughout the remaining service life of the pavement assets. Therefore, the agencies evaluate the pavement roughness at any time.

3. METHODS

Roughness occasionally exists as part of the roadway design or construction defects (Karamihas, Barnes and Rasmussen 2014), and pavement wear increases the roughness levels over time since a deformation of the pavement structure would produce a change in the road profile. Consequently, a deformation-induced increase of strain within the pavement structure must correspond to an accumulation of profile unevenness. This section first derives the theoretical relationship between the roughness condition and the accumulated strain distribution within the pavement structure along a concrete-paved road, then describes a procedure for the IRI calculation. Finally, the section introduces the previously developed connected vehicle method of roughness evaluation that the experimental study will use for validation.

3.1   The Optical Sensor

This section describes the operating principles of the optical fiber Bragg grating (FBG) sensor and its high-level construction. Because of its unique advantages of compactness, immunity to EMI and moisture, capability of quasi-distributed sensing, and long life cycle, FBG sensors have become the best candidates for long-term concrete overlay performance evaluation (Zhang, Huang and Palek, et al. 2015). Nevertheless, the basic FBG sensor, which is made of glass, is very fragile and easily damaged during concrete overlay construction. Therefore, this research team used sensors with glass fiber reinforced polymer (GFRP) packaging that ruggedized the sensors for in-pavement sensing applications.

3.1.1   Operating Principles

Figure 3.1 illustrates the operational principles of the FBG sensors. FBGs are made by laterally exposing the core of a single-mode fiber to a periodic pattern of intense ultraviolet (UV) light, which creates a fixed refractive index modulation called grating. At each periodic refraction change, a small amount of light is reflected, forming a coherent large reflection at a particular wavelength known as the Bragg wavelength. Light signals at wavelengths other than the Bragg wavelength propagate through the grating with negligible attenuation or signal variation.
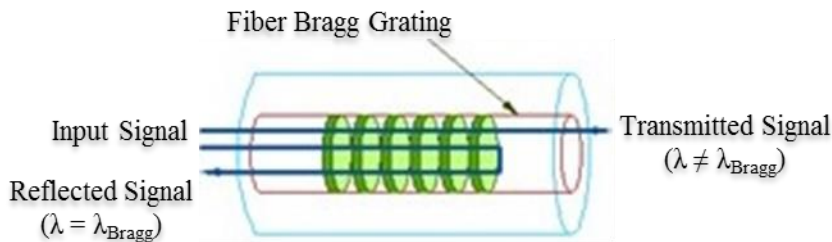
Figure 3.1 The Signal Interrogation System

The ability to accurately preset and maintain the grating wavelength is a fundamental feature and advantage of fiber Bragg gratings (Zhou, et al. 2012). Figure 3.2 shows a typical reflected spectrum of FBG. The Bragg wavelength satisfies the Bragg condition:

$$\lambda_{Bragg} = 2n\Lambda \qquad\qquad (1)$$

where n is the index of refraction and Λ is the grating periodicity of the FBG.

Due to temperature and strain dependence of the parameter, Λ, the wavelength of the reflected component will change as a function of temperature and/or strain. The general expression of the strain-temperature relationship for the FBG strain sensor and temperature compensation sensor can be described as

$$\frac{\Delta\lambda_1}{\lambda_1} = \frac{\Delta\lambda_\varepsilon}{\lambda} + \frac{\Delta\lambda_T}{\lambda_T} = (1-P_e)\varepsilon + (\alpha+\varsigma)\Delta T \tag{2}$$

where λ, ς, α, P_e, ε, and T are the resonant wavelength, thermal-optics coefficient, thermal expansion coefficient, optical elasticity coefficient, strain, and temperature, respectively. The strain after temperature compensation can then be calculated as

$$\varepsilon = \frac{1}{(1-P_e)}\left(\frac{\Delta\lambda_1}{\lambda_1} - \frac{\Delta\lambda_T}{\lambda_T}\right) \tag{3}$$
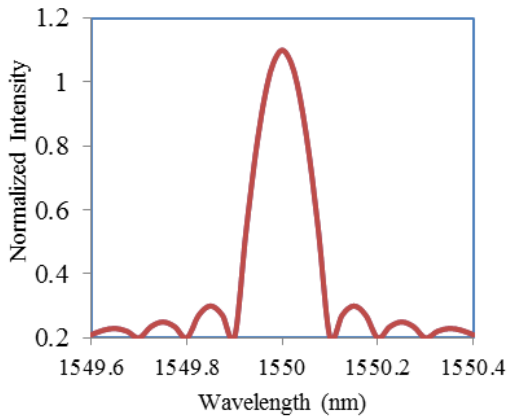
Figure 3.2 Typical Spectrum of the FBG Sensors

3.1.2 Design and Construction

The authors modified previously developed sensors (Zhou, et al. 2012) for use in this study. Both one-dimensional (1D) and three-dimensional (3D) sensor constructions are available. Figure 3.3a and Figure 3.3b show the elevation and planar views of the sensor dimensions, respectively. Figure 3.3c shows a picture by the author of the prototype. Figure 3.4 shows the dimensions of the 1D sensor. The short-gauge of the 3D sensor monitor vertical strains, whereas the long-gauges monitor the longitudinal and transverse strains inside the concrete overlays. The design modifications included a height reduction of the vertical sensor to 2.1 in. (5.33 cm) because the thickness of the concrete overlay at the test site was only 3 in. (7.62 cm). The gauge length of the 3D sensors in both the longitudinal and transverse directions are 2.2 in. (5.59 cm). The gauge length of the 1D sensor is 3 in. (7.62 cm).

6
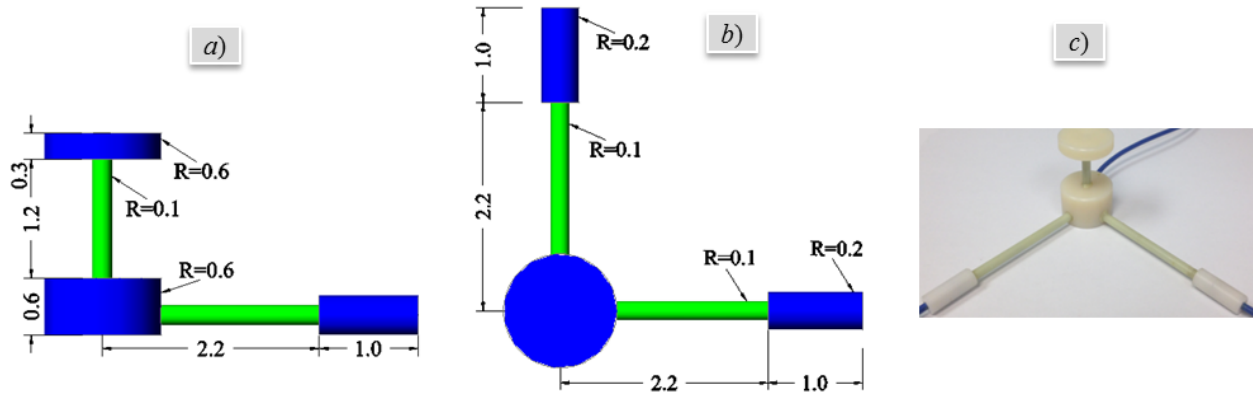
Figure 3.3 Dimensions of the 3D Optical Sensor (units: inch)

The FBG signals from all of the strain sensors were monitored in real time using an optical signal analyzer (OSA) and recorded by computers for post processing. The NI PXIe-4844 Optical Sensor Interrogator was used in this research for FBG data acquisition. The sensors had a strain sensitivity of 7.937×10^{-4} nm/με, which is the value of $1/(1-P_e)$ in Equation (3).
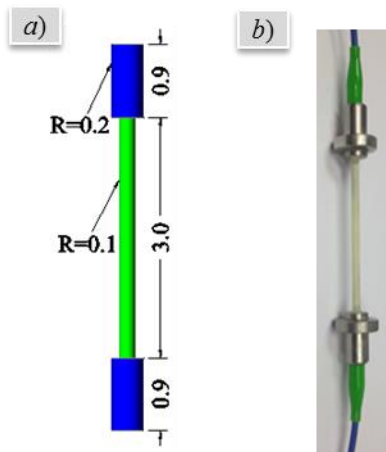
Figure 3.4 Geometric Layout of the 1D Optical Sensor (units: inch)

3.1.3 Optimization of Digital Interface

The deployed sensors must capture and report both static and dynamic loading information. Therefore, the system must be capable of digitizing the rapid strain changes that occur from passing traffic. The rolling weight of the wheel contact area across the sensors produces an analog strain signal when the vehicle traverses the sensor-embedded pavement sections. An analog-to-digital converter then immediately transforms the analog signal to digital samples that the system can store in memory or communicate to a remote system for further processing.
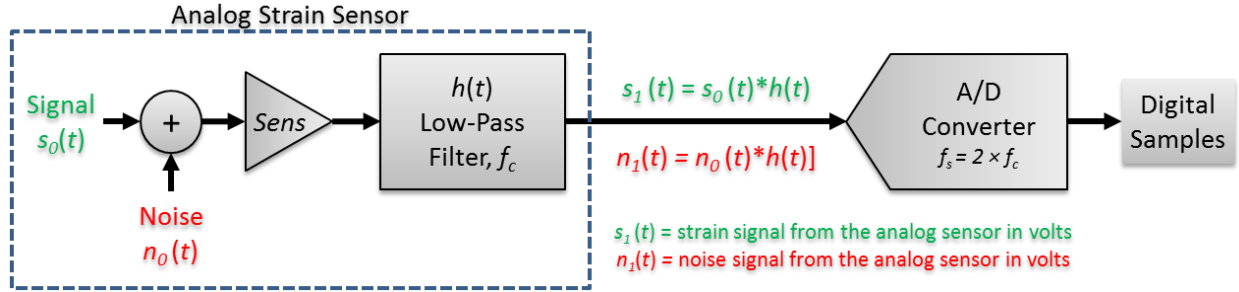
Figure 3.5 Block Schematic of the Strain Sensor System

The quality of the digital strain signal directly affects the accuracy of the measurement. The appropriate sample rate and signal-to-noise ratio will minimize strain signal distortions and maximize the measurement accuracy to distinguish the weight profile of different vehicles passing at the maximum design speed. The strain signal is a convolution of the load from the wheel contact area and the sensitivity function of the in-pavement sensors. A Fourier transform of the resulting strain signal and the Nyquist-Shannon sampling theorem provide the theoretical foundation for selecting the minimum sampling rate.

When the vehicle traverses the pavement with the embedded WIM sensor, it alters the sensor's parameters such as its electrical resistance, voltage, and light wavelength, depending on the type of sensors applied. Calibration and post processing of the effects from these parameter alternations produce the strain signal output. Therefore, the weight of the vehicle is proportional to the maximum strain values measured. Theoretically, when one vehicle tire traverses the top of the in-pavement sensor and the distance between two axles is sufficiently long to distinguish the signal from adjacent tire crossings, the sensors' strain signal becomes the convolution of the pressure distribution from the vehicle's tire contact area and the sensitivity function of the in-pavement sensor. For a specific tire, if the contact pressure $p(x, y)$ at a location (x, y) inside the contact area has a length of L_0 and a width of B_0 (Figure 3.6a) then the compressive force P of the whole tire is

$$P = \int_{L_0 \times B_0} p(x, y) ds \tag{4}$$

Integrating the contact pressure $p(x, y)$ in the lateral dimension (y direction) aligns the pressure function with the longitudinal sensitivity of the sensor, P_L, as:

$$P_L = \int_{-B_0/2}^{B_0/2} p(x, y) dy. \tag{5}$$

The longitudinally deployed sensor has a sensitivity function of S_L along the length of the sensor. The sensitivity is a function of sensor resolution, installation depth, and properties of pavement. Figure 3.6b and Figure 3.6c illustrate area-equivalent functions of the compressive force $P_L(t)$ and the sensor's sensitivity $S_L(t)$, respectively, during the traversal period.
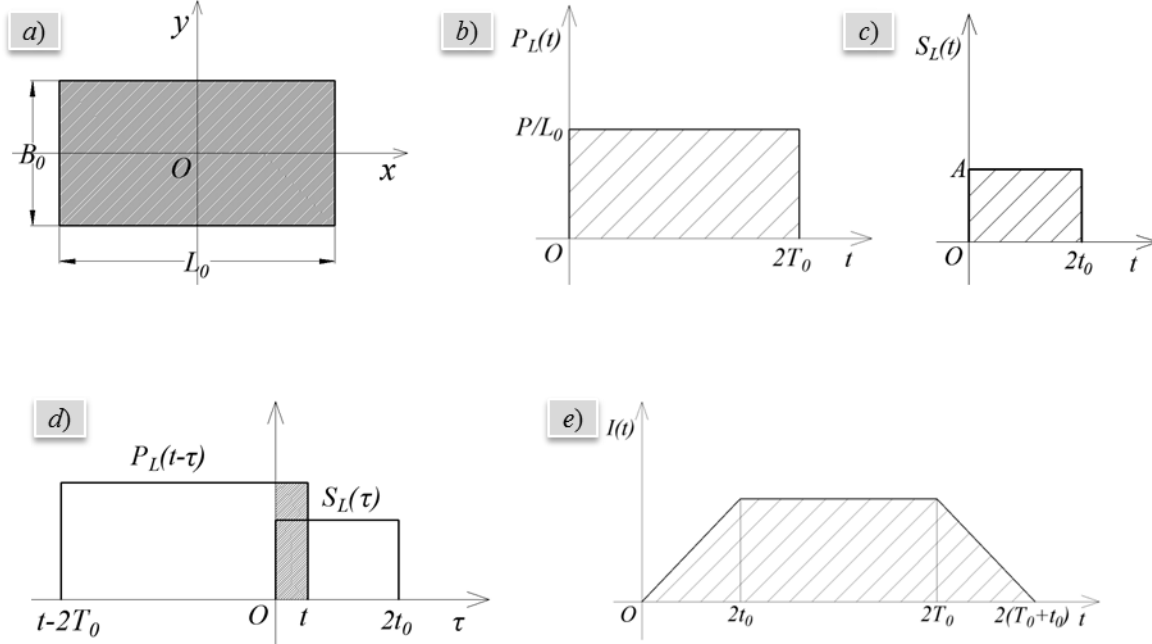
Figure 3.6 Theoretical Derivation of Minimum Sample Rate Requirement

Their respective durations $2T_0$ and $2t_0$ result from traversals at some specified speed. Therefore, the strain signal, $I(t)$, is a convolution of $P_L(t)$ and $S_L(t)$ as illustrated graphically in Figure 3.6d and Figure 3.6e:

$$I(t) = \int_{-\infty}^{+\infty} P_L(t - \tau) S_L(\tau) v \, d\tau \qquad (6)$$

such that $I(t)$ is zero outside the interval $[0, 2(T_0+t_0)]$.

The Fourier transform of the strain function in Equation (6) provides the frequency distribution to guide the selection of the optimum sampling rate. Given a finite strain signal, $I(t)$, in isolation, the Fourier transform (Chen 2004) is:

$$I(\omega) = \int_{-\infty}^{+\infty} I(t) \exp(-i\omega t) \, dt. \qquad (7)$$

The convolution property of the Fourier transform (Chen 2004) dictates that a convolution in the time domain is equivalent to a multiplication of the frequency domain functions. Thus, the Fourier spectrum of $I(t)$ is:

$$I(\omega) = v P_L(\omega) S_L(\omega). \qquad (8)$$

where $P_L(\omega)$ and $S_L(\omega)$ are the Fourier transforms of the load function $P_L(t)$ and the sensitivity function $S_L(t)$, respectively.

The frequency domain equivalent of their convolution is:

$$I(\omega) = \frac{A L_S P}{v^2} \exp[-i\omega(t_0 + T_0)] \, \text{sinc}(\omega t_0 / \pi) \, \text{sinc}(\omega T_0 / \pi) \qquad (9)$$
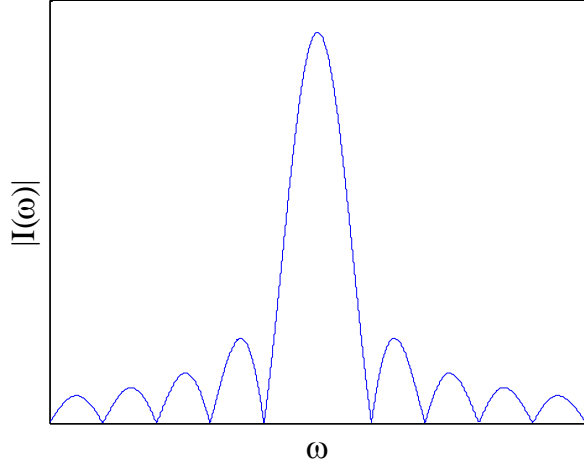
9

Figure 3.7 shows the magnitude as a function of frequency. As observed, most of the strain signal's energy is concentrated within the first lobe, termed as main lobe. The width of the main lobe was defined as its fundamental bandwidth (Chen 2004). Therefore, the fundamental bandwidth of the strain signal is:

$$B_\omega = \frac{\pi}{T_0}. \tag{10}$$

Figure 3.7 Shape of the Fourier Transform Magnitude of $I(\omega)$

Thus, in theory, the minimum sampling rate required to capture the fundamental energy of the strain signal is:

$$F_S = \frac{2B_\omega}{2\pi} = \frac{1}{T_0}. \tag{11}$$

The determination of B_ω is dependent on the comparison between T_0 and t_0 for the relative dominance of the energy within the main lobe of $I(\omega)$. The Nyquist-Shannon sampling theorem (Papoulis 1991) posits that the minimum sampling rate required to capture the signal energy is twice the strain signal bandwidth B_ω such that:

$$F_S = 2B_\omega. \tag{12}$$

This theoretical derivation of the strain signal bandwidth provides a framework to determine the minimum sample rate to support strain measurements at high vehicle speeds when using the optical sensors. The authors published a case study related to this analysis that established the minimum sample rate should be 150 Hertz to measure truck movements at 39 mph (Zhang, Huang and Bridgelall, et al. 2015).

3.2   Relating In-pavement Strains to Roughness

This research uses concrete pavements for the theoretical analysis. The analysis for other types of roads will follow similar procedures. The deformation of concrete pavement slabs commonly uses an assumption of a thin plate panel for theoretical modelling to simplify the analysis from 3D to 2D.

3.2.1 The Mechanistic Model

According to the Kirchhoff–Love plate theory (Timoshenko and Woinowsky-Krieger 1959), the strain in the longitudinal (x) direction of a thin-plate concrete panel, ε_x, located inside the pavement at some known vertical position h_0, is expressed as:

$$\varepsilon_x = -h_0 \frac{d^2 w}{dx^2},$$

(13)

where w is the vertical displacement of the concrete pavement panel, which is also known as the road elevation profile. With the sampling interval requirement satisfied, double integration of Equation (13) reproduces the relation between the road elevation profile and the measured strains from the in-pavement sensors as:

$$w = -\iint \frac{\varepsilon_x}{h_0} dx.$$

(14)

The IRI then becomes available because the slope rate of the road profile, $\ddot{w}$, which is the second derivative of the elevation profile, w, with respect to time, is a direct input to the procedure that computes the IRI. For a temporal road profile of ξ, the second derivative with respect to time is

$$\ddot{\xi} = -\ddot{w} = \frac{v^2 \varepsilon_x}{h_0}$$

(15)

where $v = 80$ km/h is the IRI standard speed (ASTM 2015).

3.2.2 The Roughness Index

The Highway Safety Research Institute (HSRI) defines the IRI in terms of the responses from a standard quarter-car model having two degrees of freedom as shown in Figure 3.8.
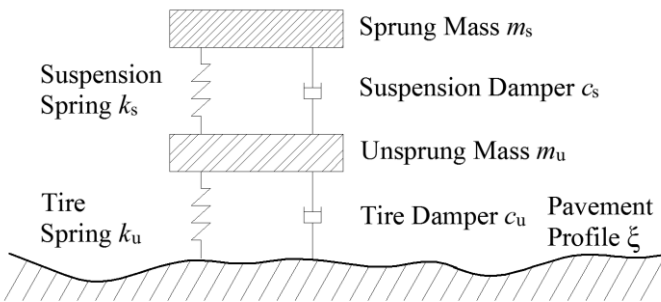
Figure 3.8 The HSRI Quarter-car Model

The parameters y^t_s and y^t_u are absolute displacements of the sprung and un-sprung mass, respectively. The HSRI quarter-car parameters are $k_u/m_s = 653.0$ s^{-2}, $k_s/m_s = 63.3$ s^{-2}, $m_u/m_s = 0.15$, $c_s/m_s = 6.0$ s^{-1} and $c_u/m_s = 0.0$ s^{-1}. Let the relative displacement of sprung mass be y_s and that of the un-sprung mass be y_u such that

$$y_s = y^t_s - y^t_u \text{ and } y_u = y^t_u - \xi. \tag{16}$$

Expressed in matrix-form, the ordinary differential equations to define the system dynamics for the sprung and un-sprung mass is

$$M\ddot{Y}(t) + C\dot{Y}(t) + KY(t) = R(t) \tag{17}$$

where

$$M = \begin{bmatrix} m_s & m_s \\ 0 & m_u \end{bmatrix}, C = \begin{bmatrix} c_s & 0 \\ -c_s & c_u \end{bmatrix}, K = \begin{bmatrix} k_s & 0 \\ -k_s & k_u \end{bmatrix}, \ddot{Y} = \begin{Bmatrix} \ddot{y}_s \\ \ddot{y}_u \end{Bmatrix}, \dot{Y} = \begin{Bmatrix} \dot{y}_s \\ \dot{y}_u \end{Bmatrix}, Y = \begin{Bmatrix} y_s \\ y_u \end{Bmatrix}, \text{ and} \tag{18}$$

$$R = \begin{Bmatrix} -m_s \ddot{\xi} \\ -m_u \ddot{\xi} \end{Bmatrix}$$

Substituting Equation (15) into the expression for R provides

$$R = \begin{Bmatrix} -m_s \dfrac{v^2 \varepsilon_x}{h_0} \\[2mm] -m_u \dfrac{v^2 \varepsilon_x}{h_0} \end{Bmatrix} \tag{19}$$

Solving Equation (17) with a numerical algorithm such as the Newmark method yields the relative displacements y_s and y_u, the relative velocities $\dot{y}_s$ and $\dot{y}_u$, and the relative accelerations $\ddot{y}_s$ and $\ddot{y}_u$ as a function of the in-pavement strains and velocities of the vehicle. The IRI is then (ASTM 2015):

$$\text{IRI} = \frac{1}{L} \int_0^T |\dot{y}_s| \, dt \tag{20}$$

in which, L is the segment length and $T = L/v$ is the travel time. For a computational sample interval of Δt, the number of intervals is $n = T/\Delta t$ and the discrete-time form of the computation becomes

$$\text{IRI} = \frac{1}{vn\Delta t} \sum_{i=0}^n |\dot{y}_s(t_i)| \Delta t = \frac{1}{vn} \sum_{i=0}^n |\dot{y}_s(t_i)| \tag{21}$$

3.3 The Connected-Vehicle Method of Roughness Evaluation

This section reviews the signal transform that fuses geospatial position, velocity, and inertial data from sensors aboard connected vehicles to produce an index that summarizes pavement roughness. The analysis characterizes the position tagging errors from conventional GPS receivers and introduces the technique to correct for those errors to localize roughness with high accuracy.

3.3.1 Sensor Signal Transform

Bridgelall [30] introduced the road impact factor (RIF) transform to summarize road roughness in direct proportion to the IRI. The RIF-index is

$$R_{\bar{v}}^L = \sqrt{\frac{1}{L} \sum_{n=0}^{N-1} \left| g_{z[n]} v_n \right|^2 \delta t}$$

(22)

where the RIF-index $R_{\bar{v}}^L$ is the average g-force magnitude experienced per unit of distance L travelled. The vertical acceleration for signal sample n is $g_{z[n]}$ and the instantaneous traversal speed is v_n. For an average sample period of δt, the average spatial resolution achievable would be $\delta L = v_n \delta t$.

The RIF-transform summarizes roughness in units of g-force per meter. It isolates the average ride roughness induced primarily from road unevenness, without including the impacts from other factors such as driver behavior and vehicle handling. Applications that need to include those other factors integrate roughness from the lateral and longitudinal accelerations using a similar model (R. Bridgelall 2013). The Ensemble Average RIF (EAR) is the average of RIF-indices from a predetermined speed band. The EAR-index represents the average roughness from road unevenness that riders experienced when traveling the segment at the average speed indicated. The speed range of a typical speed band is ±5 mph about the average speed indicated. Previous studies demonstrated theoretically and experimentally that the EAR-index and the IRI are directly proportional (R. Bridgelall 2014). Therefore, the EAR-index can extend models that currently use the IRI by calibrating them with a constant of proportionality.

3.3.2 The Roughness Indices

For multiple traversals involving one or more vehicles, an ensemble average of the RIF-indices for a selected spatial resolution window produces an estimate of the segment roughness with ever-increasing levels of precision as the traversal volume increases. The ensemble average RIF-indices (EAR) is

$$\overline{R}_{\bar{v}}^L = \frac{1}{N_{\bar{v}}} \sum_{\rho=1}^{N_{\bar{v}}} R_{\bar{v}}^L[\rho]$$

(23)

where $R_{\bar{v}}^L[\rho]$ is the RIF-index from the ρth traversal of the segment at an average speed of $\bar{v}$, and $\overline{\bar{v}}$ is the batch mean speed from all traversals of the segment. The number of available traversals for a speed band of average speed of $\bar{v}$ is $N_{\bar{v}}$. Tagging each vertical acceleration sample $g_{z[n]}$ with a geospatial position and color-coding the EAR-index will produce a map-based visualization of the segment roughness. As the precision increases with additional traversals volume, the transition between smooth and rough segments will become sharper.

3.3.3 Geospatial Position Tag Errors

The connected vehicle approach relies on *conventional* GPS receivers to tag their on-board accelerometer and velocity sensor outputs with geospatial positions. Consequently, the precision in roughness localization that is achievable depends on the performance of the underlying GPS system. Administrators of the conventional GPS system expect that the six-sigma interval for horizontal position precision under direct line-of-sight conditions will be about ±6.7 meters, which is equivalent to a standard deviation of 2.2 meters about the mean (USDHS 1996). However, this uncertainty could increase to more than ±10 meters when multi-path reflections from buildings, large trees, and other tall structures distort the weak satellite signals. Therefore, this section introduces a technique to correct for the inaccuracy of GPS position tagging by using a reference inertial marker (RIM).

The RIM may be an artificial speed bump or an existing anomaly such as a pavement patch or rough joint at a pre-determined geospatial position. Hence, the segment origin will begin at the position of the RIM. Practitioners must record its actual geospatial position on the path. This approach is analogous to the practice of placing a pneumatic tube sensor across known geospatial positions of the roadway to measure traffic volume. The speed sensor aboard a vehicle and a timer (instead of the GPS) will provide the information needed to calculate precise and continuous distance markers for the remaining inertial signal samples, relative to the path origin.

3.3.4 Roughness Localization Accuracy

The algorithm associates each inertial sample with a path distance derived from the RIM and velocity-timer measurements described above. This approach produces path distance tags with greater accuracy, particularly for curvilinear paths and turns. Therefore, the distance from any geospatial position update υ_0 is

$$\upsilon_\rho = \upsilon_0 + \sum_{n=1}^{\rho} v_n \delta t_n \tag{24}$$

where υ_ρ is the position of the ρth inertial sample update.

An RIM will produce at least one maxima in the inertial signal. Figure 3.9 compares the simulated inertial signal from traversing relatively wide and narrow isolated bumps at the speed of 67 km h^{-1} (~42 mph). The simulated inertial signal is a mathematical convolution of the quarter-car model and the vertical acceleration from traversing the elevation profile. A modified Gaussian radial bases function simulates the RIM or any bump as described in previous research (R. Bridgelall 2014).
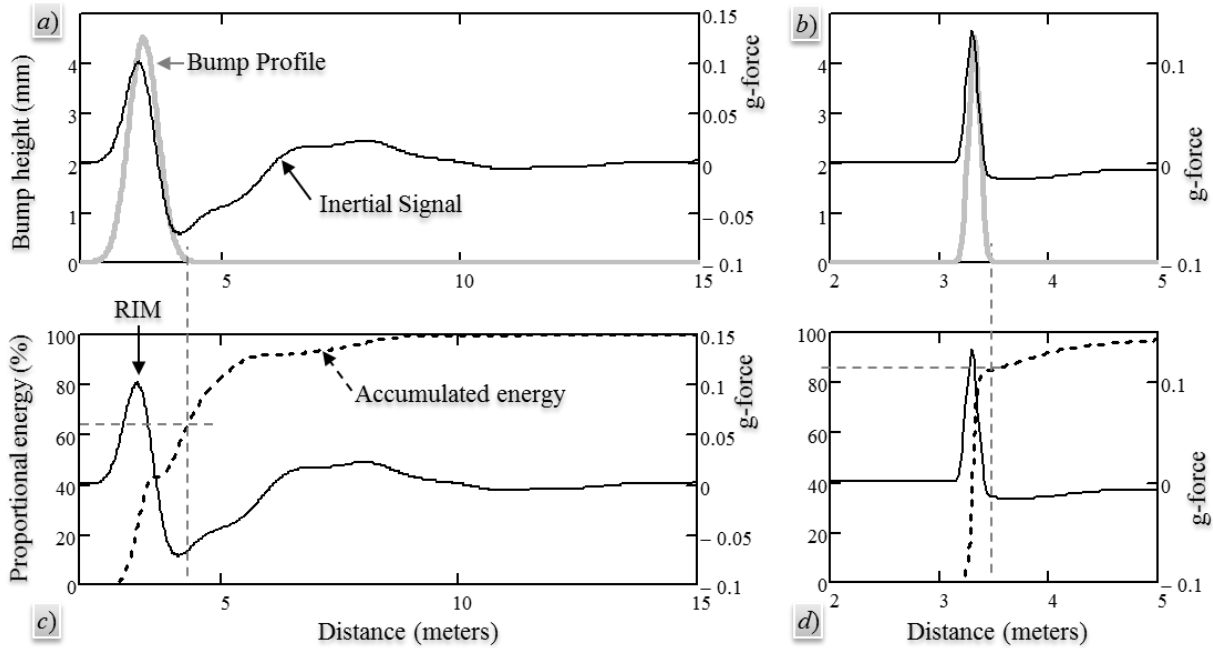
Figure 3.9 Quarter-Car Inertial Response from Wide and Narrow Bump Traversals

The position of the bump in Figure 3.9 is at a wheelbase distance of 3.3 meters from the origin. Figure 3.9a and Figure 3.9b show the g-forces that the equivalent quarter-car produces during and after traversing a 1.8-meter (6-ft.) and a 0.3-meter (1-ft.) wide bump, respectively. The bump height is 4.5 millimeters. Figure 3.9c and Figure 3.9d plots their respective proportional roughness energy accumulated as a function of distance. It is evident that most of the energy accumulates during the bump traversal and the remaining energy dissipates during the transient response after the vehicle crosses the bump.

Given the specific quarter-car, the amount of roughness energy that accumulates during the bump traversal is a function of speed and the bump width. Figure 3.10a plots the proportional roughness energy accumulated after traversing bumps with three different widths, as a function of speed. It is evident that for all cases, at least 60% of the roughness energy will accumulate during a bump traversal.
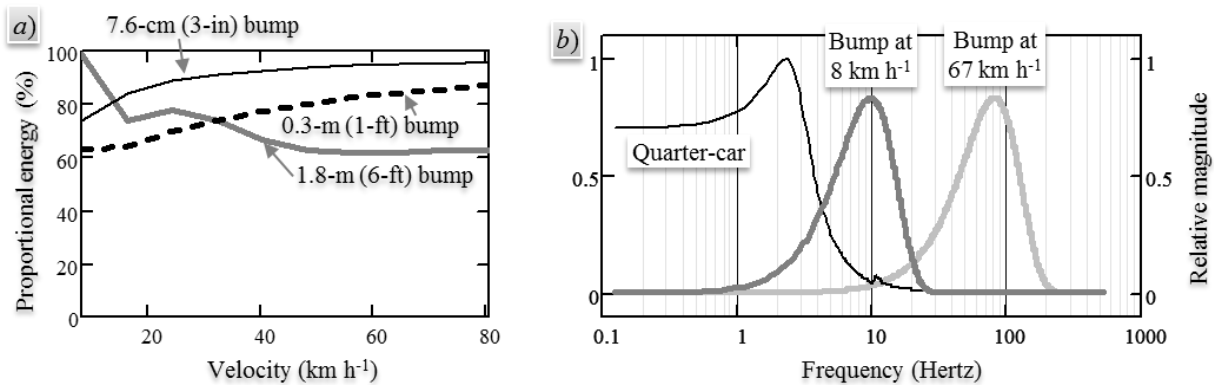
Figure 3.10 Bump Energy as a Function of Traversal Speed

15

The non-linear behavior with speed stems from the non-linear transfer-function of the quarter-car. In general, bump energy that translates with traversal speed to coincide with the un-sprung-mass mode near 10 Hertz amplifies the quarter-car response, which extends the transient response beyond the duration of the bump profile. For example, Figure 3.10b shows the frequency response of the vertical acceleration energy that the 0.3-meter wide bump produced when the vehicle traversed it at 8 km h^{-1} and 67 km h^{-1}, respectively. Traversing the bump at a lower speed moves the peak vertical acceleration energy from 90 Hertz to 10 Hertz. As implied in Figure 3.10a, the vertical acceleration energy of the 1.8-meter-wide bump translates from a lower frequency to the 10-Hertz region when the speed exceeds 40 km h^{-1}. Subsequently, any vibrations that sustain after the trailing edge of an anomaly will result in a roughness bias for the segment that immediately follows.

4. SENSITIVITY ANALYSIS

This section conducts the sensitivity study of the roughness evaluation process displayed in Section 2. The factors influencing the accuracy of the IRI estimation using the measurements from in-pavement strain sensors mainly include the implementation sensor interval and the sensor signal's quality characterized by the signal-to-noise ratio (SNR). From Equation (15), it can be seen that the in-pavement strain is directly proportional to the second derivative of the profile ($\ddot{\xi}$). The interval of the road profile samples (ξ) and the second derivative of the profile ($\ddot{\xi}$) can represent the strain sensor position intervals and the output signal of the sensors, respectively. To simulate road profiles (ξ) of different roughness levels for sensitivity analysis, the inverse fast Fourier transform (IFFT) of the PSD is a suitable approach to apply (Jiang, et al. 2012) (Wu 2000). For this analysis, the second-order forward difference provides a higher-accuracy numerical approximation of the second derivative of the profile ($\ddot{\xi}$) (Bender and Orszag 1999). After solving Equation (17) using the Newmark method, Equation (20) then provides the associated IRI for the profile. The variation in IRI is observable by changing the profile sampling interval size, which represents the strain sensor interval, for each evaluation of Equation (17). The method of noise sensitivity analysis involves adding white Gaussian noise to the in-pavement strains (ε_x), thus, to the profile's slope rate ($\ddot{\xi}$), and observing the IRI variations.

4.1 Roughness Modeling

The ISO (1995) (Andren 2005) represents the elevation profile (ξ) as a PSD such that

$$
S_\xi(\kappa) = \begin{cases} S_\xi(\kappa_0)(\dfrac{\kappa}{\kappa_0})^{-n_1} & \dfrac{\kappa}{\kappa_0} \leq 1 \\[2ex] S_\xi(\kappa_0)(\dfrac{\kappa}{\kappa_0})^{-n_2} & \dfrac{\kappa}{\kappa_0} > 1, \end{cases}
\tag{25}
$$

where, κ is the wavenumber with a unit of cycle/m, κ_0 is the datum wavenumber in cycle/m, $S_\xi(\kappa)$ is the road profile PSD in an unit of m³/cycle, and $S_\xi(\kappa_0)$ is the PSD at κ_0 or initial PSD in m³/cycle.

For typical profiles, the recommended values are $n_1=3$, $n_2=2.25$, and $\kappa_0=1/(2\pi)$ cycles/m (Cebon 1999). Table 4.1 summarizes the qualitative relationship between the roughness classification and the initial PSD. As expected, higher values of $S_\xi(\kappa_0)$ corresponds to poorer road condition in terms of roughness levels. The IRI does not respond to spatial wavelength components that fall outside of the 1.3 m to 30 m wavelength band (Gillespie, Sayers and Queiroz 1986). Therefore, the κ range from 0.02 cycle/m to 5 cycle/m is conservative for the IFFT computation. Figure 4.1 shows the road profile generated with $S_\xi(\kappa_0) = 3.2\times10^{-5}$ m³/cycle, and Figure 4.2 shows the corresponding PSD.

Table 4.1 Relationship between Roughness Classification
and Initial PSD (Cebon 1999)

Roughness Classification	$S_\xi(\kappa_0)$ 10^{-6} m³/cycle
Very Good	2-8
Good	8-32
Average	32-128
Poor	128-512
Very Poor	512-2048
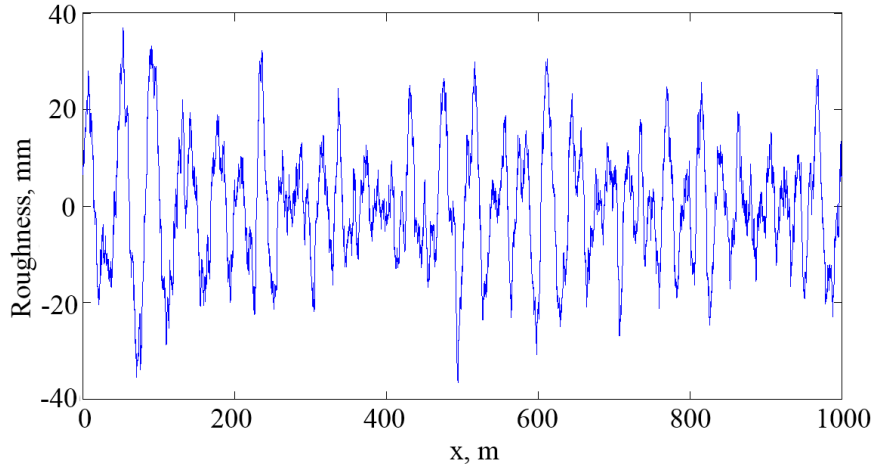
Figure 4.1 Generated Road Profile at $S_\xi(\kappa_0) = 3.2\times10^{-5}$ m³/cycle
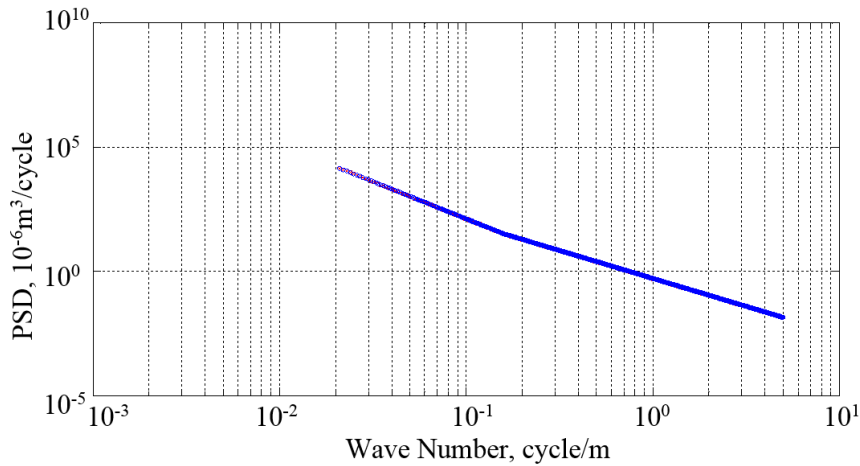
Figure 4.2 Profile Power Spectral Density at $S_\xi(\kappa_0) = 3.2\times10^{-5}$ m³/cycle

4.2   Sensitivity to In-pavement Sensor Interval

The Nyquist-Shannon sampling theorem dictates a minimum profile sampling interval of 0.65 m because the IRI becomes insensitive to wavelengths shorter than 1.3 m. Figure 4.3 shows the change of IRI with the sensor interval for the roughness generated at $S_\xi(\kappa_0) = 3.2\times10^{-5}$ m³/cycle. As shown in Figure 4.3, the IRI steadily decreases as sensor interval increases. The tradeoff between IRI accuracy and in-pavement strain sensor interval directly relates to the expense of sensor installation. The recommended standard sampling interval is 0.3 meters using the vehicle based profiling approaches (ASTM 2015). However, installing strain sensors at the equivalent sampling intervals would require a significantly large number of strain sensors that would result in a high initial installation cost.

18
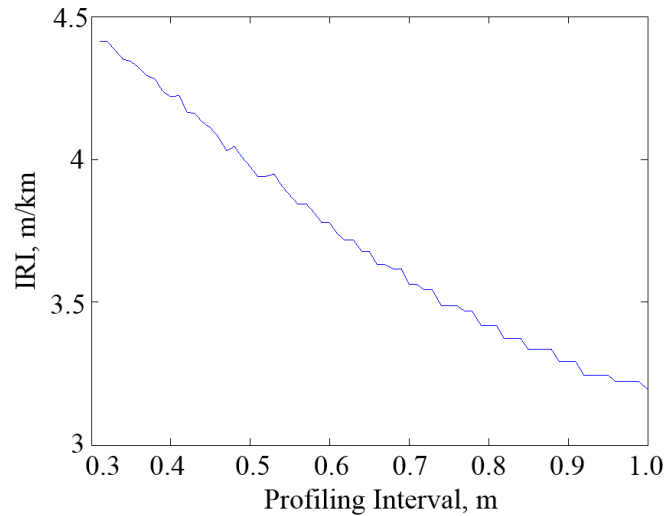
Figure 4.3 IRI at Different Strain Sensor Intervals

To potentially reduce the number of sensors needed for a more cost-effective solution, Table 4.2 compares various sensor intervals for different levels of roughness $S_\xi(\kappa_0)$ with measurement accuracies of 90% and 80% compared with the IRI calculated from standard intervals of 0.3 m. The results indicate that larger IRI or rougher surfaces require fewer sensors. Since the road roughness matter more when the IRI increases, users can increase the sensor interval to decrease cost without losing measurement accuracy. A sensor interval of 0.7~0.8 m would provide an accuracy within 80% for roughness levels that correspond to the road conditions with average or below that matter most to the agencies. Hence, trading off 20% accuracy reduces the required number of in-pavement strain sensors by at least a factor of two. For specific applications, a sensor interval analysis is highly recommended before the sensor installation.

Table 4.2 Sensor Intervals Required for an Accuracy of 80% and 90%

$S_\xi(\kappa_0)$, 10^{-6} m^3/cycle	2	4	8	16	32	64	128	256	512	1024	2048
IRI at 0.3 m, m/km	1.1	1.6	2.2	3.2	4.6	6.3	8.9	12.8	17.9	25.0	36.1
Sensor Interval (90% Acc.), m	0.3	0.3	0.3	0.4	0.4	0.5	0.5	0.5	0.5	0.5	0.5
Sensor Interval (80% Acc.), m	0.4	0.5	0.6	0.6	0.7	0.7	0.8	0.7	0.7	0.8	0.8

4.3   Sensitivity to Sensor Signal Quality

This section uses the ASTM Standard E 1926-98 (ASTM 2015) profile with known IRI to study the noise sensitivity of the in-pavement strain sensor on IRI estimation. Figure 4.4 shows the simulated standard sinusoidal road profile. Table 4.3 lists the calculated IRI values and the relative errors for different levels of white Gaussian noise. The relatively small error of 5.0% between the IRI of the ASTM profile and the IRI computed from generating the slope rate estimated from the strain-based method in this paper validates the method. Adding noise levels ranging from 3 dB to 10 dB to the slope rate of the profile estimated from the strain-based approach results in relative errors that are less than 5% as listed. This result demonstrates that the developed strain-based roughness estimation method is relatively insensitive to noise.
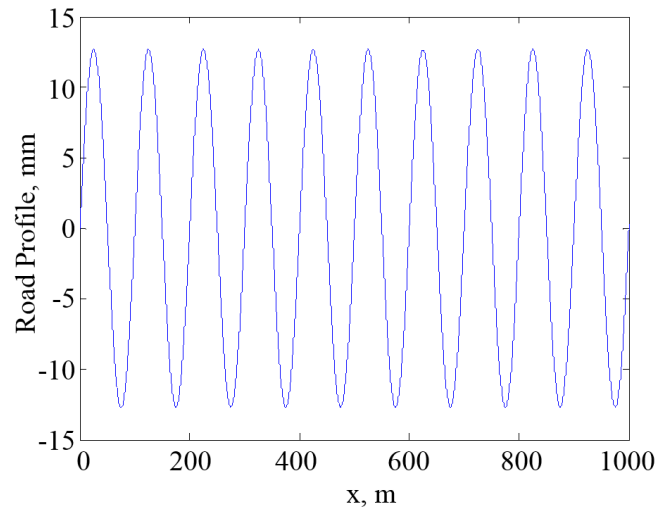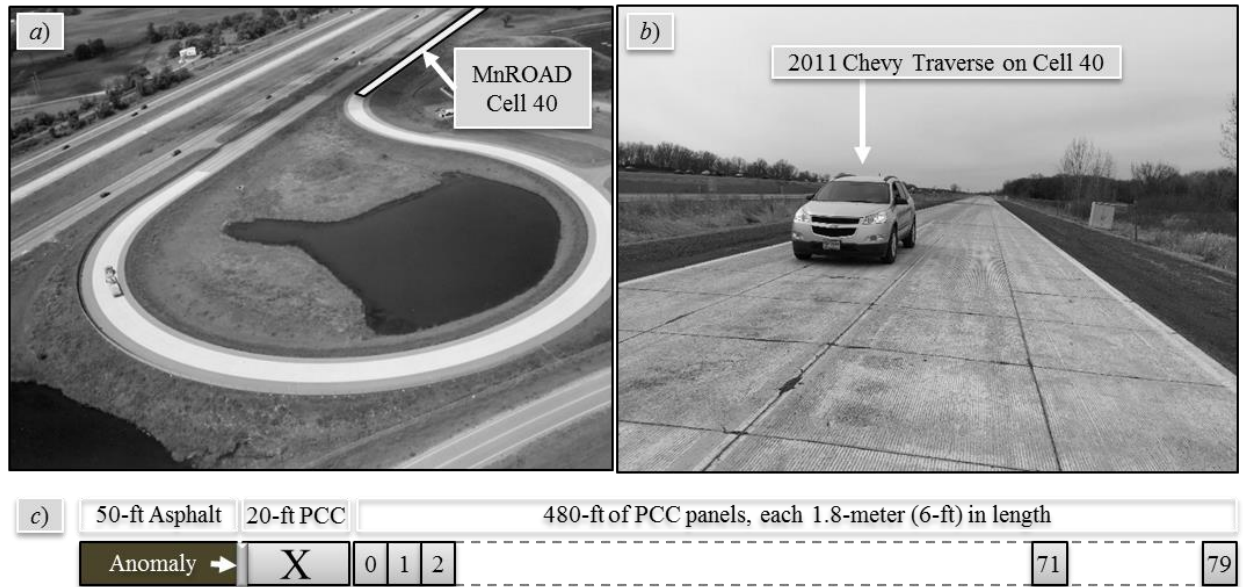
Figure 4.4 Road Profile based on ASTM Standard E 1926-98 (ASTM 2015)

Table 4.3 Validation of the Method for IRI Calculation

Parameter	ASTM	Proposed Strain-based Method			
		No Noise	3 dB Noise	8 dB Noise	10 dB Noise
IRI	0.0222	0.0211	0.0226	0.0216	0.0215
Relative Error	-	5.0%	1.8%	2.7%	3.2%

5.   RESULTS AND DISCUSSIONS

Figure 5.1 Road Sections at MnROAD for Roughness Evaluation

The high-resolution localization feature of the connected-vehicle method of roughness characterization provided validation for the in-pavement strain sensor method. The Minnesota Department of Transportation (MnDOT) owns and operates a road section of the Cold Weather Road Research Facility in Minnesota (MnROAD) that contains various in-pavement strain sensors. MnROAD consists of two unique roadways: a two-lane, low-volume loop that is loaded with a five-axle 80,000 lb. (36,287 kg) semi, and a section of Interstate I-94 ''mainline'' that contains two westbound lanes with live traffic. Figure 5.1a shows the two roadway sections and the Cell-40 test site. Figure 5.1b shows the Portland cement concrete (PCC) panels selected for roughness evaluation. As illustrated in Figure 5.1c, Cell 40 begins with a 15.2-meter (50-ft.) asphalt pavement section followed by a 6.1-meter (20-ft.) PCC panel, and then 80 shorter 1.8-meter (6-ft.) panels, numbered as shown. The rough joint (anomaly) between the asphalt and PCC sections serve as the RIM.

The rest of this section describes the field tests, analyzes the results, and finally validates the strain-based method using the connected vehicle approach.

5.1   Roughness Estimation Using the In-pavement Strain Sensors

This method measures the accumulated strains during the simulated traffic on the road section and calculates the present roughness level (IRI) using the method developed in Section 2.

5.1.1   Experimental Setup

The authors' research group previously developed multiple glass fiber reinforced polymer packaged fiber Bragg grating (GFRP-FBG) sensors and installed them within three panels of Cell 40 at MnROAD. Figure 5.2a shows a picture by the author of the 1D sensor installation in Panel 36, and Figure 5.2b shows a picture of the installation in Panel 40.
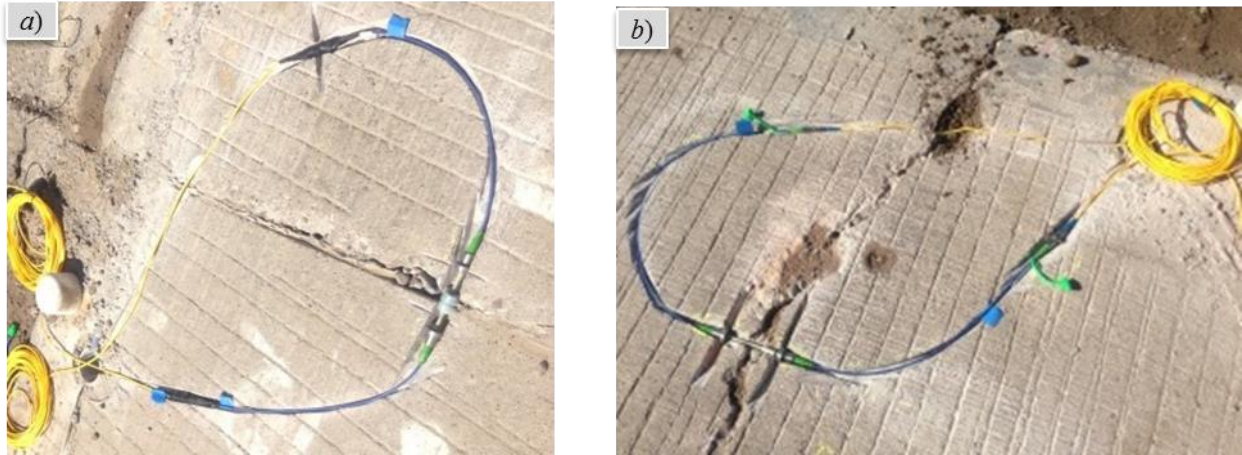
Figure 5.2 Sensor Deployment in Concrete Pavement Panels of the Test Site

The associated reference (Zhou, et al. 2012) provides details of the design and installation procedures. Panels 36, 40, and 53 embedded the GFRP-FBG sensors as shown in the layout in Figure 5.3. The three panels contained sensors that measure strains in one dimension (1D), and panels 36 and 40 contained one additional sensor each that can measure strains in three dimensions (3D). The sensors were located above a 0.5-in. (13 mm) elevation level relative to the bottom surface of the pavement panel, and along the truck wheel path. The orientations o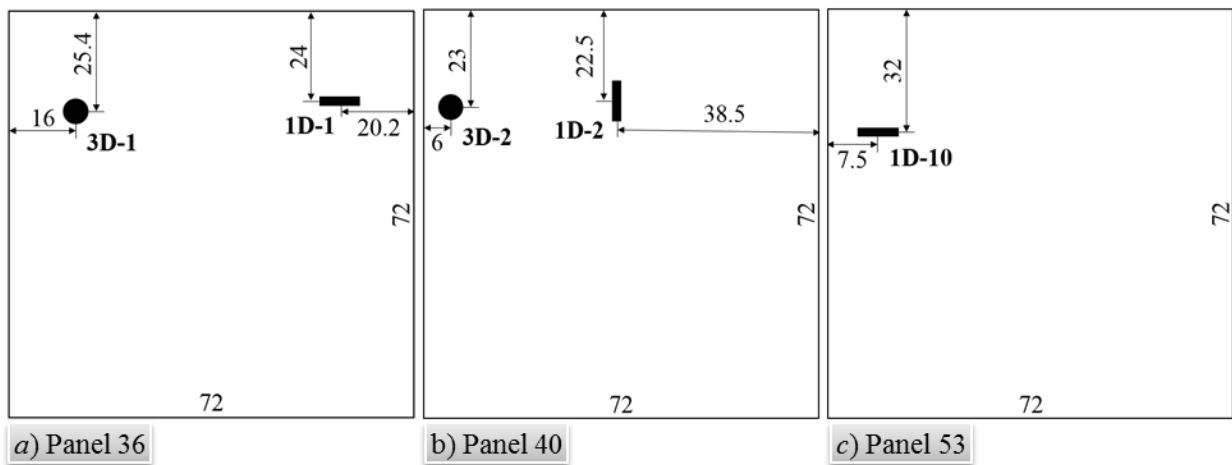f the 1D and 3D sensors are as indicated in Figure 5.3. This experiment used only the longitudinal component of the three orthogonal sensors of the 3D version for strain measurements. In addition, a temperature tree installed on the side of each panel provided data to compensate for environmental effects on the strain measurements.

**Figure 5.3** Sensor Layout at the Pavement Panels (Unit: inches)

To assess the mechanical effect from truck loading, all sensors are embedded along the wheel path. High performance polymer bonds the sensor to the existing concrete pavement.

5.1.2 Results and Analysis

After temperature compensation, the analysis treats the strain distribution along the wheel path of each panel as step functions (Figure 5.4).
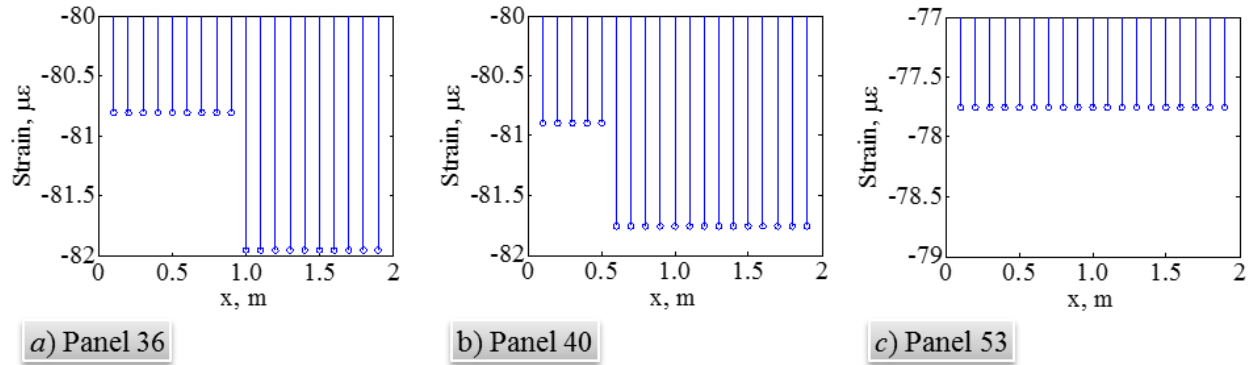
Figure 5.4 Strain Distribution along the Wheel Path Track of Each Testing Panel

The first transition point is equidistant to the sensor's position from the panel edge. The orientation of the 1D sensor within Panel 40, 1D-2, is in the traverse direction. The history of the strain values from the three sensors indicates that the analysis need not differentiate between values in the longitudinal and transverse directions (Zhang, Huang and Palek, et al., Glass fiber–reinforced polymer–packaged fiber Bragg grating sensors for ultra-thin unbonded concrete overlay monitoring 2015) for static strain measurements. As Panel 53 has a single sensor, there will be no transition points. The sampling intervals between strain sensor positions are 0.9 m for Panel 36, 0.7 m for Panel 40, and 1.8 m for Panel 53. Following the procedure in Section 2 for the strain-based method, the estimated IRI values are 2.00, 2.01, and 1.92 for Panel 36, Panel 40, and Panel 53, respectively. According to the sensitivity study on sensor interval summarized in Table 4.2, the accuracy of estimated IRI for the Panel 36 and 40 are around 80% and that for Panel 53 will be less than 80%. This is within expectations because the single sensor of Panel 53 must produce a larger error than for the other two panels that contain two sensors each that shorten the interval between samples.

5.2   Roughness Estimation Using the Connected-Vehicle Method

This study used a regular passenger vehicle, a 2011 Chevrolet Traverse (Figure 5.1b), to collect the inertial and geospatial position data needed for the RIF-transform. Three smartphones secured flat in the vehicle's rear trunk ran a data logger application (app) that produced inertial and geospatial position data from at least 30 traversals of Cell 40. The smartphones contain the same sensors as a connected vehicle and, therefore, served as a proxy. The velocity sensor of a connected vehicle is likely more accurate. Therefore, the results when using actual connected vehicles are likely to be even better.

5.2.1 Field Testing Using the Connected-Vehicle Approach

Figure 5.5a shows a top view of the smartphone installation, and Figure 5.5b illustrates the orientation references. Phone 1 and Phone 2 were iPhone® 4S devices fixed in the longitudinal orientation, whereas Phone 3 was an iPhone® 5 oriented in the lateral direction. The GPS receiver had an update rate of 1 Hz and the accelerometer was set to sample at 128 Hz based on recommendations from prior studies (R. Bridgelall 2014). The iOS® app logged inertial and geospatial position data as the vehicle traversed the PCC panels selected for roughness evaluation.
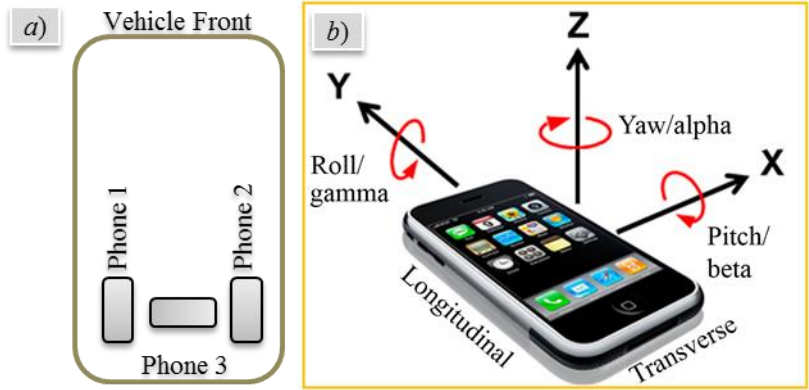
Figure 5.5 Smart Phone Installation at the Rear Trunk for Field Testing

5.2.2 Experimental Results and Analysis

A comma separated value (CSV) file format is the recommended organization for RIF-transform data as shown in Table 5.1. The first row contains a header with labels for each column of data sampled from the inertial and geospatial sensors on the smart phones. The integrated timer provides the "Time" data in milliseconds. The integrated GPS receiver provides the latitude (L_{at}) and longitude (L_{on}) data in decimal format, and the ground speed (G_{speed}) in m/s. The integrated inertial sensor provides the accelerator values for the g-forces sensed in the vertical, lateral, and longitudinal directions as "G_z," "G_x," and "G_y," respectively, and normalized to 9.81 m/s^2. The integrated gyroscope produces the "Pitch," "Roll," and "Yaw" for the sensor orientation angles in degrees, respectively.

Table 5.1 Standard Data Format Used to Compute RIF

Time	Gz	Lat	Lon	Vel	Pitch	Roll	Yaw	Gx	Gy
21.347	-0.98	46.88096	-96.7701	1.42	8.19	1.51	-25.61	0.05	-0.13
23.956	-1.02	46.88096	-96.7701	1.42	8.17	1.51	-25.63	0.05	-0.14
26.118	-0.99	46.88096	-96.7701	1.42	8.17	1.51	-25.63	0.02	-0.15
37.812	-1.03	46.88096	-96.7701	1.42	8.17	1.50	-25.64	0.05	-0.12
48.627	-0.97	46.88096	-96.7701	1.42	8.17	1.50	-25.64	0.08	-0.14
59.410	-1.02	46.88096	-96.7701	1.42	8.16	1.55	-25.67	0.00	-0.16
123.741	-0.95	46.88096	-96.7701	1.42	8.20	1.47	-25.73	0.02	-0.13
134.777	-1.05	46.88096	-96.7701	1.42	8.20	1.47	-25.73	0.04	-0.15

Figure 5.6a plots the inertial signal from two randomly selected data streams of the traversal data set. The signal shape that contains the RIM is a response that is familiar from the simulated bump traversal (Figure 3.9). It is evident that the RIM position tags vary significantly among traversals because of the GPS error. The RIF-transform with a spatial resolution window equal to a panel length (1.8-meters) produced the associated sequence of RIF-indices shown for the first inertial signal (Figure 5.6a).
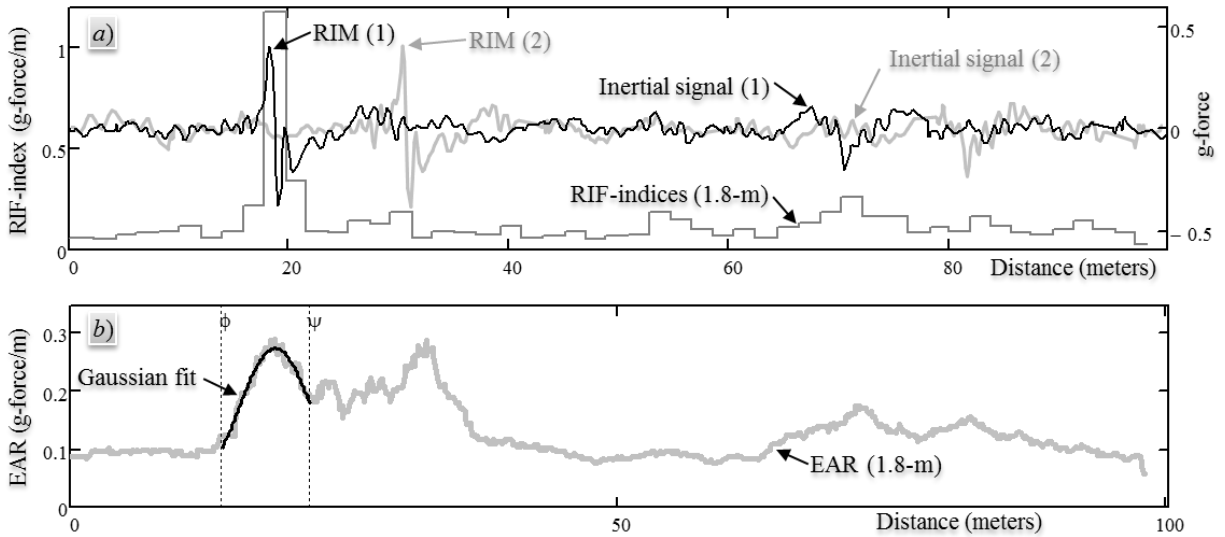
**Figure 5.6** RIF-Indices and their Position Distribution

Figure 5.6b plots the EAR using Equation (23) with the same spatial resolution window. The EAR reveals a multi-modal distribution of the position tags. Figure 5.6b also overlays a least squares fit of the Gaussian distribution around the first EAR peak (between the position markers φ and ψ). Additional research related to this dataset provides further details about the statistical distribution observed (Bridgelall, et al. 2016).

Using a spatial resolution window of 1.8 meters for the RIF-transform, Figure 5.6 compares the EAR for the GPS-tagged and the RIM-aligned inertial samples. It is evident that in addition to delaying the localized roughness of the reference anomaly, the random distribution of the GPS position tags smears the localized roughness measurements. Therefore, relative to the RIM-aligned method, the EAR-indices of the GPS-tagged method could result in more than a twofold error in measuring the localized roughness of a Cell 40 PCC panel. However, the roughness measurement error of the GPS-tagged method will match those of the RIM-aligned method as the size of the spatial resolution window increases well beyond the uncertainty interval of the GPS position estimates.
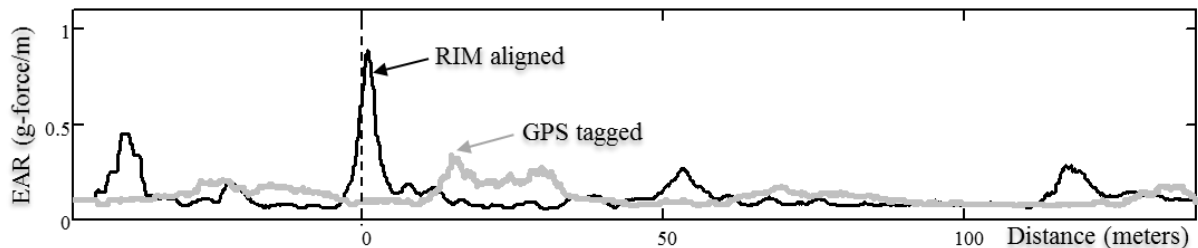
Figure 5.7 The EAR for the RIF-transform of GPS-tagged and RIM-aligned inertial samples

Figure 5.8 shows the EAR-indices, based on the RIM-aligned EAR, for each PCC panel. The EAR-index for the three panels deployed with the in-pavement strain sensors are 0.149, 0.162, and 0.144 for Panel 36, Panel 40, and Panel 53, respectively.
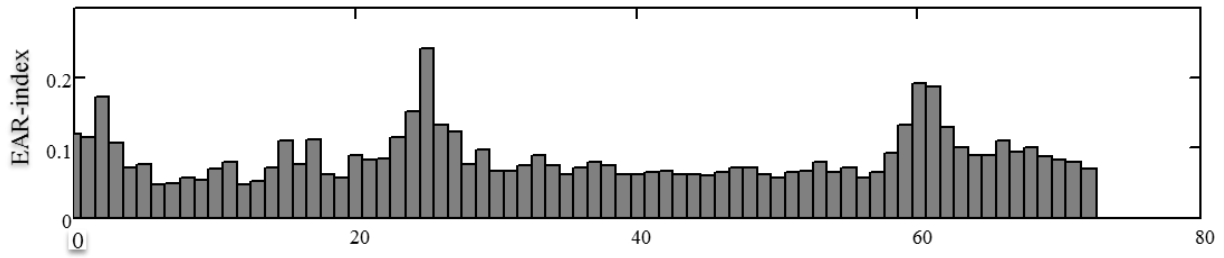
Figure 5.8 EAR-indices for the PCC Panels of Cell 40

5.3   Validation of Strain Sensor Roughness Estimation Method

The high cost of traditional methods for obtaining the IRI presents a significant barrier to validating the developed strain-based method in this paper by using a laser-based profiler vehicle. However, the direct proportionality relationship between the IRI and the EAR-index provides a cost-effective means of validating the proposed roughness estimation method using in-pavement strain sensors by comparing it with the respective roughness indices obtained from the connected vehicle approach, localized to the three panels.Table 5.2 compares the estimated IRI using the strain-based method and the obtained EAR-indices from the connected-vehicle method for Panel 36, Panel 40, and Panel 53 and their ratios. The ratios of the IRI to the EAR-indices for the three panels range from approximately 12 to 14. The estimated IRI is proportional to the EAR-indices at an average ratio of 13.04. The standard deviation of the ratios is only 3.3% of the mean. This indicates a high degree of consistency in the two methods. This result validates the effectiveness of estimating the IRI using the in-pavement strain sensors.

Table 5.2 Comparison of IRI and EAR-index on Sensor-Deployed Panels

	Panel 36	Panel 40	Panel 53
IRI derived from strain-based method	2.00	2.01	1.92
EAR-index from the connected-vehicle method	0.149	0.162	0.144
IRI/EAR-index	13.40	12.43	13.31

26

6.   CONCLUSIONS

This study provides transportation researchers and engineers with a cost-effective method of road roughness evaluation using strain sensors deployed inside the pavement. The authors conducted theoretical and numerical analysis to develop the relationship between strains measured using the in-pavement sensors and the IRI. The field experiments validated the theoretical development. The conclusions of this research are as follows:

1)   The strain series that develop gradually and accumulate with road use is directly proportional to the second derivative of the road elevation profile. The procedure that produces the IRI is a linear time-invariant transformation of the second derivative of the road elevation profile. Therefore, the IRI is directly proportional to the strain data.

2)   Numerical simulation proves that a measurement accuracy of at least 80% is achievable using the strain-based method at a sensor placement interval of at least 0.7 meters to report roughness levels that are of most significance to agencies. The analysis also determined that the strain-based sensing method is relatively insensitive to the noise disturbances.

3)   The case studies using strain sensor data collected from three concrete panels in the field validated the new roughness evaluation method by comparing the consistency of its proportionality with the connected-vehicle method of roughness localization. Previous work demonstrated that the connected vehicle method is directly proportional to the IRI.

4)   The connected vehicle technique of localized roughness measurements that use reference inertial markers can correct for a twofold increase in localized roughness measurements that GPS-related errors accumulate.

A fusion of the in-pavement sensors and the connected vehicle method of localized roughness measurements will enable in-pavement optical sensors to monitor continuously pavement mechanistic parameters, traffic load parameters, as well as roughness indices. The results of this research indicates that future in-pavement sensors would be capable of providing greater utility than previously imagined. That is, a single sensor type can measure and report many of the most important parameters needed to assess pavement condition, usage characteristics, and performance throughout their life cycle. The steady cost reduction of optical fiber sensors and the steady pace of connected vehicle adoption will enable practitioners to accelerate the pace of smart city developments. Agencies can select the optimum mix of the two scalable and intelligent monitoring solutions for continuous, network-wide assessment of performance and maintenance needs. This approach is synergistic with the development of autonomous vehicles. For example, future implementations would allow vehicles to communicate with the embedded sensors to aid navigation in bad weather. In future work, the authors will explore those ideas and also extend the method for road condition monitoring and traffic data collection.

7.   REFERENCES

Abaynayaka, S. W., H. Hide, G. Morosiuk, and R. Robinson. 1976. *Tables for estimating vehicle operating costs on rural roads in developing countries.* Victoria: Transport and Road Research Laboratory (TRRL).

Al-Omari, Bashar, and Michael I. Darter. 1994. "Relationships between international roughness index and present serviceability rating." *Transportation Research Record* (National Academies of Science) (1435): 130-136.

Andren, Peter. 2005. "Power spectral density approximations of longitudinal road profiles." *International Journal of Vehicle Design* (Inderscience Publishers) 40 (1-3): 2-14.

ASTM. 2015. *Standard practice for computing International Roughness Index of roads from longitudinal profile measurements.* ASTM Standard E1926-08, West Conshohocken, Pennsylvania: American Society for Testing Materials (ASTM).

ASTM. 1998. *Standard practice for computing ride number of roads from longitudinal profile measurements made by an inertial profile measuring device.* ASTM E1489, West Conshohocken, Pennsylvania: American Society for Testing Materials (ASTM).

—. 1997. *Standard Terminology Relating to Vehicle-Pavement Systems.* Standard E867. West Conshohocken, PA: American Society of Testing and Materials (ASTM).

Bender, Carl M., and Steven A. Orszag. 1999. *Advanced mathematical methods for scientists and engineers* . Springer Science & Business Media.

Brickman, Arthur Donald, W. H. Park, J. C. Wambold, and J. R. Zimmerman. 1972. *Road roughness effects on vehicle performance.* Report No. TTSC 7207, University Park: Pennsylvania State University.

Bridgelall, R., Y. Huang, Z. Zhang, and F. Deng. 2016. "Precision enhancement of pavement roughness localization with connected vehicles." *Measurement Science and Technology* (IOP Publishing) 27 (2): 025012.

Bridgelall, Raj. 2014. "A participatory sensing approach to characterize ride quality." *Proceedings of SPIE Volume 9061, Sensors and Smart Structures Technologies for Civil, Mechanical, and Aerospace Systems.* Bellingham, Washington: International Society for Optics and Photonics (SPIE). doi:10.1117/12.2046854.

Bridgelall, Raj. 2014. "Connected Vehicle Approach for Pavement Roughness Evaluation." *Journal of Infrastructure Systems* (American Society of Civil Engineers) 20 (1): 04013001 (1-6). doi:10.1061/(ASCE)IS.1943-555X.0000167.

Bridgelall, Raj. 2014. "Inertial Sensor Sample Rate Selection for Ride Quality Measures." *Journal of Infrastructure Systems* (American Society of Civil Engineering) 21 (2): 04014039 (1-5). doi:10.1061/(ASCE)IS.1943-555X.0000225.

Bridgelall, Raj. 2015. "Precision bounds of pavement deterioration forecasts from connected vehicles." *Journal of Infrastructure Systems* (American Society of Civil Engineers) 21 (1): 04014033 (1-7).

—. 2013. "RAILCOTS -- Rolling Stock Automatic In-Situ Line-Quality, Car Operations and Tracking System." *Sensors Expo & Conference.* Chicago, IL: Questex.

Brown, Doug, Wei Liu, and T. F. Henning. 2010. *Identifying pavement deterioration by enhancing the definition of road roughness.* Wellington, New Zealand: New Zealand Transport Agency.

Carey, William N. Jr., and Paul E. Irick. 1960. *The Pavement Serviceability - Performance Concept.* Bulletin 250, National Research Council, Washington, D.C.: Highway Research Board, 40-58.

Cebon, D. 1999. *Handbook of vehicle–road interaction.*

Chen, Chi-Tsong. 2004. *Signals and Systems.* 3rd. New York: Oxford University Press.

Darter, Michael I., and Ernest J. Barenberg. 1976. *Zero-maintenance pavement: Results of field studies on the performance requirements and capabilities of conventional pavement systems.* FHWA-RD-76-105 Interim Report, Washington, D.C.: Federal Highway Administration.

Deusen, B.D. Van. 1967. *Analytical techniques for designing riding quality.* Technical Paper 670021, Warrendale, PA: Society of Automotive Engineers.

Gillespie, T. D., and M. Sayers. 1981. "Role of road roughness in vehicle ride." *Transportation Research Record* (Transportation Research Record 836) 836: 15-20.

Gillespie, T. D., M. W. Sayers, and C. A. V. Queiroz. 1986. *The International Road Roughness Experiment: Establishing Correlation and Calibration Standard for Measurement.* Technical Report No. 45, Washington, D.C.: The World Bank, 464.

Huang, Yang Hsien. 1993. *Pavement analysis and design.* Englewood Cliffs, New Jersey: Prentice-Hall, Incorporated.

Hyman, William Albert, A. D. Horn, O. Jennings, F. Hejl, and T. Alexander. 1990. *Improvements in data acquisition technology for maintenance management systems.* NCHRP Report 334, Washington, D.C.: Transportation Research Board.

Jiang, Cao Dong, Lin Cheng, Sun Fengchun, and Chang Hongjie. 2012. "Simulation of road roughness based on using IFFT method." *Software Engineering (WCSE), 2012 Third World Congress on.* Institute of Electrical and Electronic Engineers. 190-193.

Kajner, Lyle, Marian Kurlanda, and Gordon Sparks. 1996. "Development of Bayesian regression model to predict hot-mix asphalt concrete overlay roughness." *Transportation Research Record: Journal of the Transportation Research Board* (National Academies of Science) (1539): 125-131.

Karamihas, Steven M. 2016. *Measuring, Characterizing, and Reporting Pavement Roughness of Low-Speed and Urban Roads.* Research in Progress, Washington, D.C.: Transportation Research Board of the National Academies. Accessed October 12, 2015. http://apps.trb.org/cmsfeed/TRBNetProjectDisplay.asp?ProjectID=3404.

Karamihas, Steven M., Michelle A. Barnes, and Robert O. Rasmussen. 2014. *Pavement surface specification for road load measurement.* UMTRI-2014-9, Ann Arbor, Michigan: University of Michigan Transportation Research Institute (UMTRI) .

Klaubert, Earl C. 2001. *Highway effects on vehicle performance.* FHWA-RD-00-164, Washington, D.C.: Federal Highway Administration (FHWA).

Marcondes, Jorge, Gary J. Burgess, R. Harichandran, and Mark B. Snyder. 1991. "Spectral Analysis of Highway Pavement Roughness." *Journal of Transportation Engineering* 117 (5): 540–549.

McGhee, Kenneth H. 2004. *Automated pavement distress collection techniques.* NCHRP Synthesis 334, Washington, D.C.: National Cooperative Highway Research Program (NCHRP).

McKenzie, David, and Maitree Srinarawat. 1978. *Root Mean Square Vertical Acceleration (RMSVA) as a basis for Mays meter calibration.* Brazil Project Technical Memo BR-23, Austin, Texas: University of Texas at Austin.

Papoulis, Athanasios. 1991. *Probalility, Random Variables, and Stochastic Processes.* New York: McGraw-Hill.

Paterson, William. 1989. "A transferable causal model for predicting roughness progression in flexible pavements." *Transportation Research Record* (National Academy of Science) (1215): 70-84.

Saleh, Mofreh, Michael Mamlouk, and Emmanuel Owusu-Antwi. 2000. "Mechanistic roughness model based on vehicle-pavement interaction." *Transportation Research Record: Journal of the Transportation Research Board* (National Academy of Sciences) 1699: 114-120.

Schram, Scott, and Magdy Abdelrahman. 2006. "Improving prediction accuracy in mechanistic-empirical pavement design guide." *Transportation Research Record: Journal of the Transportation Research Board* (National Academies of Science) (1947): 59-68.

Sebaaly, Peter E., Stephen Lani, and Adam Hand. 1995. "Performance models for flexible pavement maintenance treatments." *Transportation research record* (National Academies of Science) (1508): 9-21.

Smith, K. L., K. D. Smith, L. D. Evans, T. E. Hoerner, M. I. Darter, and J. H. Woodstrom. 1997. *Smoothness specifications for pavements.* NCHRP Project 1-31, Washington, D.C.: National Cooperative Highway Research Program (NCHRP).

Timoshenko, Stephen P., and Sergius Woinowsky-Krieger. 1959. *Theory of plates and shells.* London: McGraw-Hill.

Wu, Jiunn-Jong. 2000. "Simulation of rough surfaces with FFT." *Tribology International* (Elsevier) 33 (1): 47-58.

Yu, H. T., K. D. Smith, M. I. Darter, J. Jiang, and L. Khazanovich. 1998. *Performance of concrete pavements. Volume III: Improving concrete pavement performance.* FHWA-RD-95-111, Washington, D.C.: Federal Highway Administration.

Zhang, Zhiming, Ying Huang, Leonard Palek, and Robert Strommen. 2015. "Glass fiber–reinforced polymer–packaged fiber Bragg grating sensors for ultra-thin unbonded concrete overlay monitoring." *Structural Health Monitoring* 14 (1): 110-123.

Zhang, Zhiming, Ying Huang, Leonard Palek, and Robert Strommen. 2015. "Glass fiber–reinforced polymer–packaged fiber Bragg grating sensors for ultra-thin unbonded concrete overlay monitoring." *Structural Health Monitoring* (Sage Journals) 14 (1): 110-123.

Zhang, Zhiming, Ying Huang, Raj Bridgelall, Leonard Palek, and Robert Strommen. 2015. "Sampling optimization for high-speed weigh-in-motion measurements using in-pavement strain-based sensors." *Measurement Science and Technology* (IOP Publisher) 26 (6): 065003.

Zhiming, Zhang, Ying Huang, Raj Bridgelall, Leonard Palek, and Robert Strommen. 2015. "Sampling optimization for high-speed weigh-in-motion measurements using in-pavement strain-based sensors." *Measurement Science and Technology* (IOP Publishing) 26 (6): 065003.

Zhou, Z., W. Q. Liu, Y. Huang, H. P. Wang, M. H. Huang, and J. P. Ou. 2012. "Optical fiber Bragg grating sensor assembly for 3D strain monitoring and its case study in highway pavement." *Mechanical Systems and Signal Processing* 36-49.